communications earth & environment

ARTICLE

https://doi.org/10.1038/s43247-023-01169-7 OPEN

Widespread diffuse venting and large microbial iron-mounds in the Red Sea

Froukje M. van der Zwan [1✉], Nico Augustin [2], Sven Petersen [2], Sharifah M. Altalhi[1,3], Júnia Schultz[1], Raquel S. Peixoto [1], Jörg Follmann[1], Arthur Anker[1], Francesca Benzoni [1], Evelyn R. Garcia Paredes [1], Murtadha Al Malallah[1], Lera Shepard [1], Mustapha Ouhssain[1], S. Beatrice Jägerup[1], Burton H. Jones [1] & Alexandre S. Rosado [1]

For decades, hydrothermal activity along the Red Sea Rift was only inferred from metalliferous sediments and hot brines. Active hydrothermal fluid discharge was never directly observed from this young ocean basin, but could be key to understanding the evolution of hydrothermal vent fields and associated life. Here we report the discovery of widespread diffuse venting at Hatiba Mons, the largest axial volcano in the Red Sea. The active vent fields are composed of iron-oxyhydroxide mounds, host thriving microbial communities and are larger and more abundant than those known from any other (ultra) slow-spreading mid-ocean ridge. Diffuse venting, controlled by intense faulting, and the lack of vent-specific macrofauna, are likely causes for the abundant microbial mats that dominate and built up the hydrothermal mounds. These microbe-rich hydrothermal vent fields, occurring in a warm ocean, may be analogous to Precambrian environments hosting early life and supporting the formation of large iron deposits.

[1] King Abdullah University of Science and Technology (KAUST), Thuwal, Saudi Arabia. [2] GEOMAR Helmholtz Centre for Ocean Research Kiel, Kiel, Germany. [3] Taif University, Taif, Saudi Arabia. ✉email: froukje.vanderzwan@kaust.edu.sa

Magmatically driven hydrothermal circulation of seawater through the crust takes place along all mid-ocean ridges[1], often forming mineral deposits and habitats for chemosynthetic life at the seafloor[2,3]. Since their discovery[4], numerous studies of active hydrothermal vents and diverse chemosynthetic communities have increased our understanding of marine biodiversity and the history of life[5–8]. However, the evolutionary aspects and colonization processes of hydrothermal vents are still poorly constrained[9], particularly for young, enclosed oceans such as the Red Sea.

Seafloor spreading in the Red Sea between the Nubian and Arabian plates began at ~13 Ma[10,11]. The oldest oceanic crust is, however, buried under Miocene evaporites and younger sediments[12,13]. The exposed oceanic crust is younger than ca. 5 Ma in the southern Red Sea and 2–3 Ma in the central Red Sea[14–16]. In the central Red Sea, typical ultraslow-spreading rift morphologies occur in wide troughs and basins (the Red Sea Deeps)[17,18] that are separated by evaporite- and sediment-filled inter-trough zones[13,19].

Hydrothermal activity in the Red Sea has been associated with brine pools, hosting metalliferous sediments that were discovered in the 1960s[20]. Since then, abundant research on the brines provided indirect evidence for hydrothermal influx into some of the brines, based on their elevated temperatures (up to 68 °C), their chemical compositions[21,22], and the presence of metalliferous sediments[20,23,24]. The source of hydrothermal venting could, however, not be confirmed by visual observations due to the harsh conditions of the brines for modern equipment. The only in-situ sulfide chimney observations in the Red Sea have been reported from Kebrit Deep, where they occur along the brine-seawater interface[25]. These inactive chimneys, consisting of iron (Fe)-, lead (Pb)-, and zinc (Zn)-sulfides, are interpreted to have precipitated from 110-130 °C hydrothermal fluids. Other sulfide fragments were reported from the rift valley at 18°N but without vent observations[26]. Hydrothermal venting has thus never been directly observed in the Red Sea, although vent fields are expected to occur based on global distribution statistics[27]. Further evidence for extensive hydrothermal activity along the Red Sea Rift axis comes from basalt trace element chemistry, particularly chlorine has been used to indicate hydrothermal activity[28–30]. High chlorine contents in basalt samples from the Red Sea Rift suggest that hydrothermal circulation is actually widespread. Since these analyses also point to locations with a high potential for the presence of hydrothermal vents, they also reveal areas of particular interest for further exploration[31,32]. The discovery of active sites in the Red Sea is important because the ultraslow-spreading rate (<10 to >16 mm/yr)[33,34] combined with overall elevated heat flow and salinity[32,35] may lead to extensive massive sulfide formation[36,37], as supported by the discovery of the largest modern hydrothermal submarine metal deposit in the Atlantis II brine[23,38,39]. Further, due to the Red Sea being semi-enclosed, its bottom water is saltier (~40‰ vs. 35‰ global average)[40] and 18 °C warmer (21.7 °C vs. 2–4 °C)[41,42] than that in other oceans, requiring adaption of deep-sea organisms. The closest (low-T) hydrothermal site occurs in the Gulf of Aden[43,44] south of the narrow and shallow connection of the Red Sea to the Indian Ocean. Here, no vent-specific faunal communities have been reported[45]. The distinctive seawater characteristics of the Red Sea and limited connectivity to the rest of the global mid-ocean ridge system may prevent colonization by deep-sea species from the Indian Ocean[46]. This, together with a reset of the Red Sea ecosystem resulting from a major extinction event during the last glacial maximum, ~20,000 years ago[47], formed a unique ecosystem in the Red Sea, with a very high amount of endemic species[48]. Hence, chemosynthetic communities at hydrothermal vent fields may also be unique and the Red Sea could play a key role in understanding the evolution of vent fauna in young ocean basins, with implications for understanding migration of species between hydrothermal vents. Finally, the salinity and temperatures of the Red Sea bottom water[41] are possibly closer to those of Precambrian oceans that had higher salinities and overall higher temperatures than most present-day oceans[49,50]. Therefore, the deep Red Sea may simulate conditions encountered by Earth's early life[51] or during the formation of large Banded Iron Formations, which are considered fossil remains of early life[52].

Here, we report the discovery of widespread hydrothermal discharge at Hatiba Mons volcano in the Red Sea Rift, where diffuse low-temperature (low-T) venting has created numerous Fe-oxyhydroxide mounds. We also present geomorphological and tectonic interpretations of the geological setting, bulk chemistry of hydrothermal precipitates, as well as a preliminary description of the associated vent biome of this new hydrothermal system. We use these data to draw conclusions on the environmental conditions during the vent field formation and evolution.

Results and discussion

Hydrothermal vent fields at Hatiba Mons volcano. Hatiba Mons is the largest submarine axial volcano in the central Red Sea, with a basal diameter of 11.4 km, a height of 530 m, and an estimated age of 1 Ma[14]. It erupts typical mid-ocean ridge basalts that are also comparable to other samples from the Red Sea Rift (Supplementary Tables 1 and 2)[31]. Hatiba Mons is strongly faulted and the major normal faults show a distinct hourglass-shaped pattern crosscut by a radial fault pattern (Fig. 1). This pattern results from a combination of regional rifting and the volcano's local stress field over a hot mantle[53]. Recent magmatic activity is indicated by low local seismicity[10,54], as well as by high multibeam-backscatter[13,14], ROV observations, and the presence of fresh basaltic glasses that all suggest lava flows with an age of <1000 yr old (Fig. 2, Supplementary Fig. 1a). This recent magmatic activity, the high chlorine contents of nearby basalts[31,32] and its low summit magnetization[55] related to hydrothermal alteration[56], make Hatiba Mons a prime target for hydrothermal exploration on the Red Sea Rift.

CTD casts, MAPR tow-yo's, and AUV water column data reveal a number of turbidities and minor Eh anomalies over the summit, indicating abundant hydrothermal venting (see Methods, Supplementary Fig. 2). High-resolution (2 m) AUV bathymetry data of the summit area show smooth but heavily faulted terrain (average fault density > 1×10^2 m/m^2; Fig. 1, Supplementary Fig. 3). Morphologically distinct irregularly-shaped areas ($n = 45$) with a high rugosity and a generally low backscatter intensity were also identified (Figs. 1 and 2, Supplementary Fig. 1). Of these, 14 were confirmed to be of hydrothermal origin by ROV observations and sampling (Figs. 2 and 3, Supplementary Fig. 4). Assuming all these areas are hydrothermal fields, their total surface covers 1.6 km^2, with individual fields having dimensions of 50–1000 m (Fig. 2, Supplementary Tables 3 and 4). AUV sub-bottom profiling of four of these fields showed that they lie directly on the volcanic basement with similar average thicknesses of 4.8–6.4 m (Supplementary Fig. 5, Supplementary Table 4). The total estimated volume of the Hatiba Mons hydrothermal deposits is 9.3×10^6 m^3 (Supplementary Table 2).

Each field comprises a series of mounds frequently aligned in ridges. Both features are associated with faults and fissures but are not faulted themselves (Fig. 2). The hydrothermal fields are generally not directly associated with the youngest lava fields. Individual mounds are up to 40 m in diameter, while elongated ridges can reach up to 150 m in length (Fig. 2). The mounds are up to 10 m high, with an average of 3–5 m (Supplementary Table 4). Most mounds are dome to cone-shaped with rough,

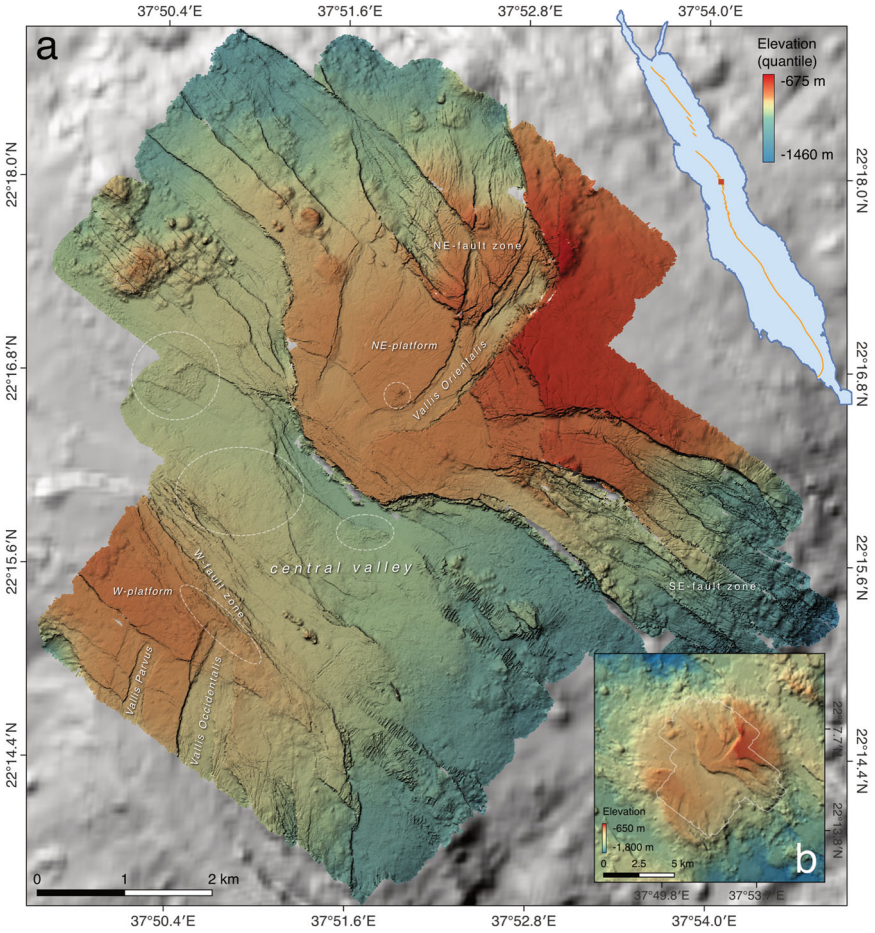

Fig. 1 Hatiba Mons AUV Bathymetry. a High-resolution AUV-derived bathymetry (color coded) of the summit of Hatiba Mons volcano in the central Red Sea Rift (over ship-bathymetry, shaded gray[14]). The dashed circles indicate the areas with the largest hydrothermal fields (see Fig. 2). **b** The inset shows the entire volcano and the limits of the AUV data (white line) superimposed on ship bathymetry. The position of the volcano within the context of the Red Sea (top right inset) at the rift axis (red line[10]) is shown by the red square.

steep slopes (Figs. 2 and 3). Mound surfaces are encrusted with layered slabs and botryoidal or irregular crusts and dm-sized chimneys, while sediments cover the areas between the mounds (Fig. 3). Venting of clear fluids was observed at several locations with shimmering fluids rising at least 1 m above the chimneys into the water column at *Farwah Safraa* ridges (Fig. 3c). The abundance of microbial colonies on all mound fields surveyed by ROV suggests diffuse venting is widespread. Temperature measurements of hydrothermal fluids and sediment are up to 40 °C (Supplementary Fig. 4) but represent a minimum due to the imprecise placement of the T-loggers by the ROV. Nevertheless, the presence of bacterial colonies directly at the openings of active vents chimneys implies that the fluids there have temperatures below 121 °C, the present upper limit for life[57]. This does not exclude, however, higher temperatures deeper in the system, as mixing with seawater at or below the seafloor may occur.

Samples of hydrothermal crust and chimneys are layered and vary in color from black and red-brown to yellow and green (Fig. 4a). Optical and scanning electron microscopy (SEM) imaging of the crusts reveals microbe-like forms such as (interweaving) filaments, twisted stalks, and spheroidal structures (Fig. 4b–f). X-ray diffractometry shows that the chimneys and crusts consist mainly of amorphous compounds with traces of crystalized todorokite (Mn-oxide; Supplementary Table 2). Some greenish-yellow crust samples contain the clay mineral nontronite (Fig. 4a, Supplementary Table 2). Sulfides are absent from the current sample set. Anhydrite was also not observed, which agrees with the current temperature assumptions (anhydrite is only stable >150 °C[58]). The bulk of the crust material consists of a mixture of Fe- and Mn-oxyhydroxides, with some samples showing an abundance of siliceous material and/or Ca-carbonate from background sedimentation (Fig. 5a, Supplementary Table 2). Bulk rock major and trace element chemistry of the crusts shows high inter-sample compositional variability, similar to observations from other low-T vent locations globally ($n = 13$; Fig. 5a, Supplementary Table 2). Chemical data from our precipitates cover the full range of existing literature data, and the chemistry is directly related to the color of the samples, reflecting their major mineralogy (Fig. 5a, Supplementary Table 2). Some samples contain high concentrations of Ba (up to 1740 ppm), Zn (up to 1220 ppm), and elevated concentrations of the trace metals As, Pb, Sb, Tl, and Hg, indicating that fluid temperatures in the subseafloor were high enough to leach and transport those metals from below. However, the concentrations of metals that are usually associated with black-smoker-style high-T venting, such as Cu and Se, are very low (Supplementary Table 2). Uranium, Ni, Mo, and V concentrations are elevated but can be explained by scavenging from seawater[59].

Biodiversity of the Hatiba Mons hydrothermal fields. Yellow to white microbial mats occur in varying abundances in all surveyed vent fields and are most abundant at southern *Farwah Safraa* ridges, *Baja'ah Mounds*, and *Majarrah Mounds* (locally up to 20–90% of a hydrothermal mound, Supplementary Table 4). The

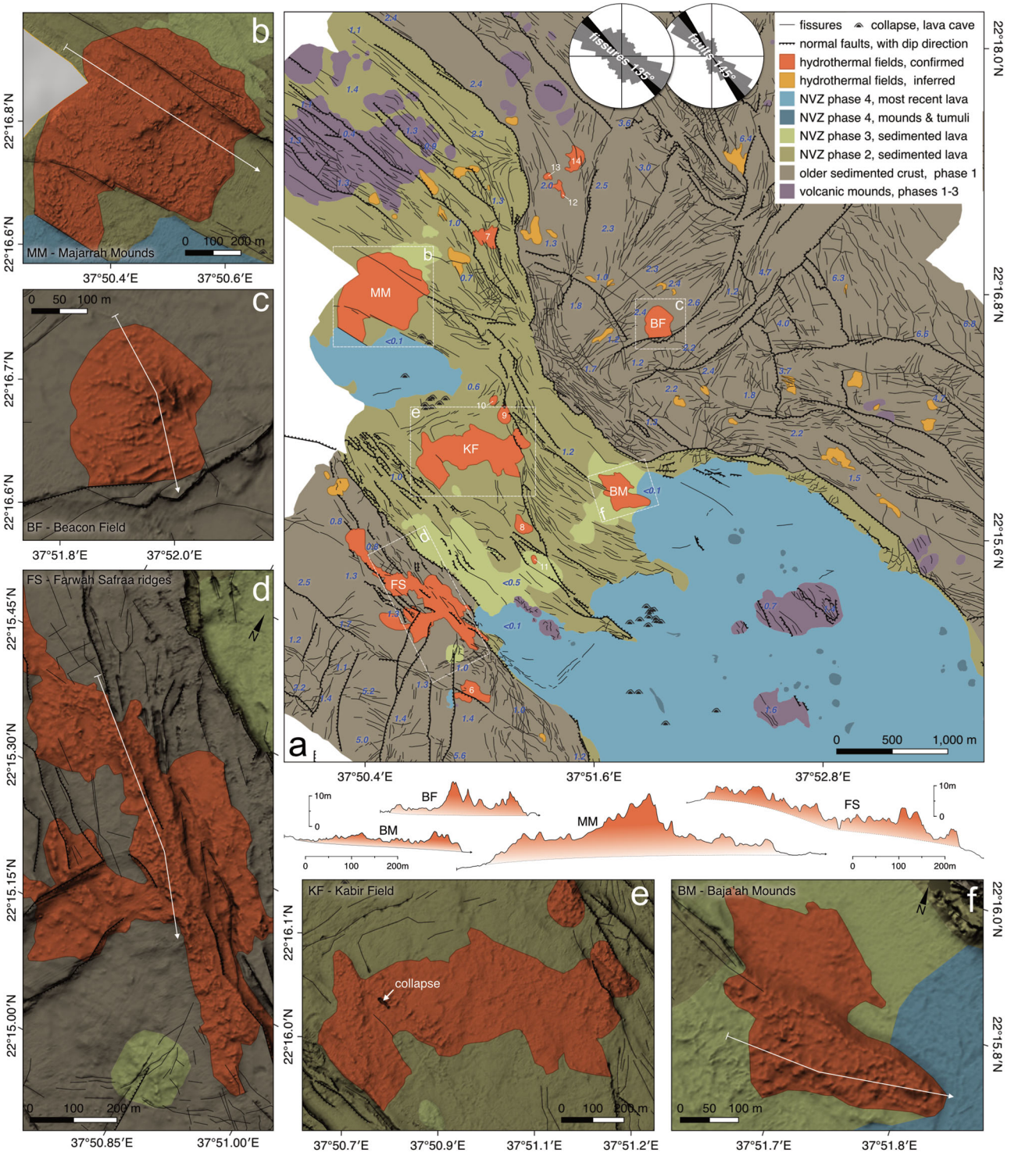

Fig. 2 Geological map of Hatiba Mons and detailed views of the largest hydrothermal fields. a The geological interpretation is based on AUV and ship bathymetry, AUV sub-bottom data, multibeam backscatter, ROV observations, and seafloor sampling. The largest lava flow covers a total area of about 57×10^6 m^2 and extends up to 16 km southeastwards (AUV combined with ship bathymetry). AUV bathymetry indicates its thickness is ~2.5 m, and thus, the flow has a total volume of 142×10^6 m^3. The sediment thickness across Hatiba Mons is variable and shown in blue numbers (meters, from AUV sub-bottom data and ROV observations). Based on sediment thickness and backscatter intensity, four eruption phases with different ages are identified. Phase 1 is the oldest, most sedimented, and faulted lava on the uplifted volcanic flanks. Phases 2–4 all occur in the neo-volcanic zone (NVZ) of the rift and have decreasing amounts of sediments, indicating a decrease in age from phase 2 to 4. The primary strike directions of normal faults and fissures are 145° and 135°, respectively, coinciding with the main spreading direction of the Red Sea overlain by local stress patterns caused by the weight of the volcano. **b**–**f** Each hydrothermal field comprises a series of mounds that frequently form elongated ridges aligned with the underlying fissures and cracks. The profiles of the hydrothermal fields are comparable in vertical and horizontal scales, and white lines mark their positions. The largest fields are **b** Beacon Field (BF), **c** Majarrah Mounds (MM), **d** Farwah Safraa ridges (FS), **e** Baja'ah Mounds (BM), and **f** Kabir Field (KF).

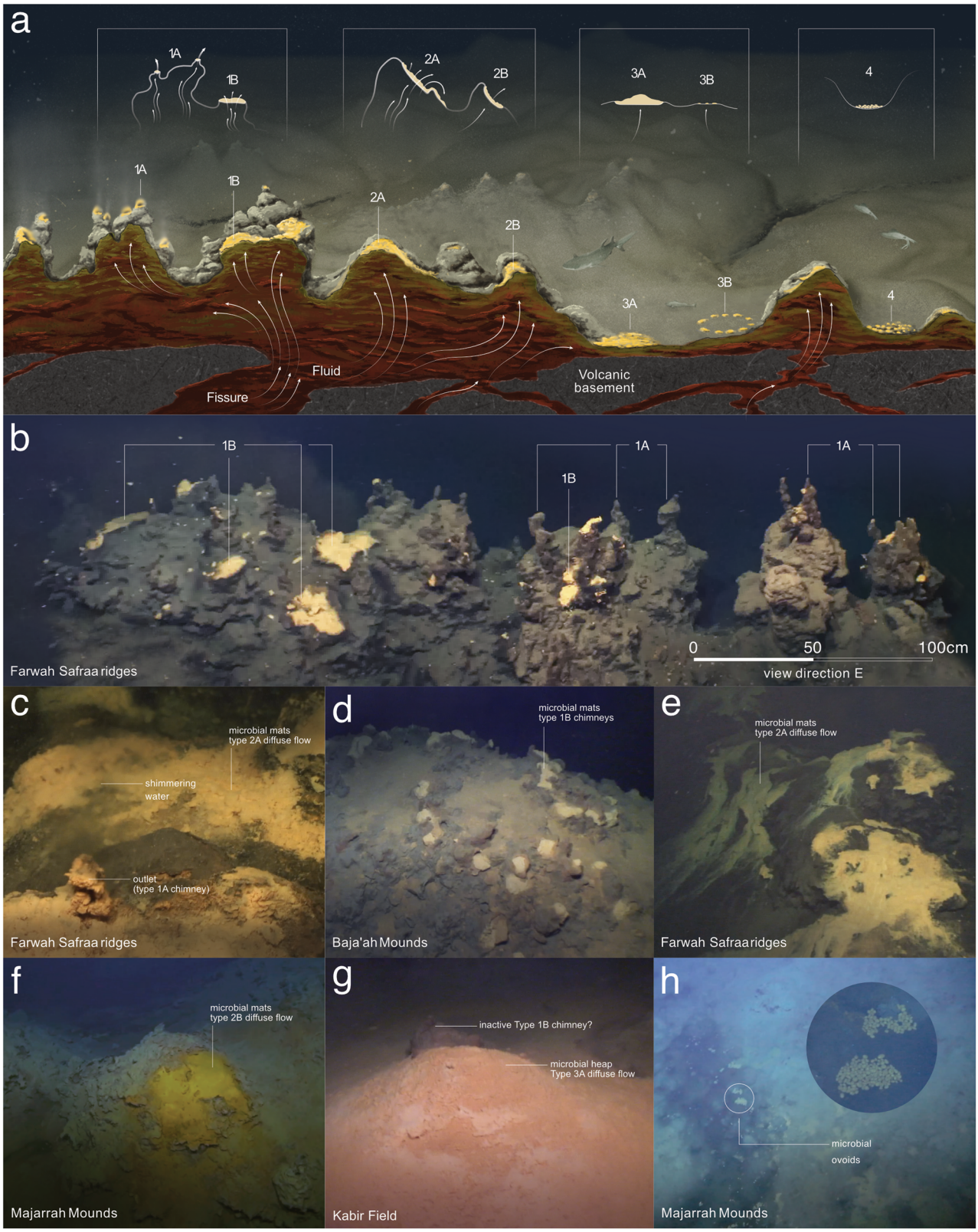

Fig. 3 Types of hydrothermal vents, mounds, and microbial mats at Hatiba Mons. a Conceptual drawing and summary of the low-T hydrothermal occurrences found at the Hatiba Mons volcano based on ROV images, AUV bathymetry, sub-bottom profiling, and seafloor sampling. **b**–**h** Typical seafloor structures within the low-T hydrothermal fields at Hatiba Mons. **b**–**d** Type 1 vents with focused flow, characterized by dm-sized chimneys (type 1A) or elevated bowl-like structures (type 1B). **e**, **f** Diffuse type 2 outflow with voluminous, fur-like, and thick fluffy microbial mats with a downhill-flow appearance (type 2A) or less voluminous microbial mats (type 2B). **g** Type 3 venting is characterized by smaller microbial heaps in areas of very diffuse flow in the valleys or flat surfaces (3A). **h** Type 4 ovoids or rolls of bacteria within discolored sediment (type 3B). Concept image by Ivan Gromicho, KAUST. Seafloor images **b**–**e**, **g** were taken with the MaxRover ROV (HCMR) in May 2022. Images **c** and **h** were taken with Fugro ROV in February 2022.

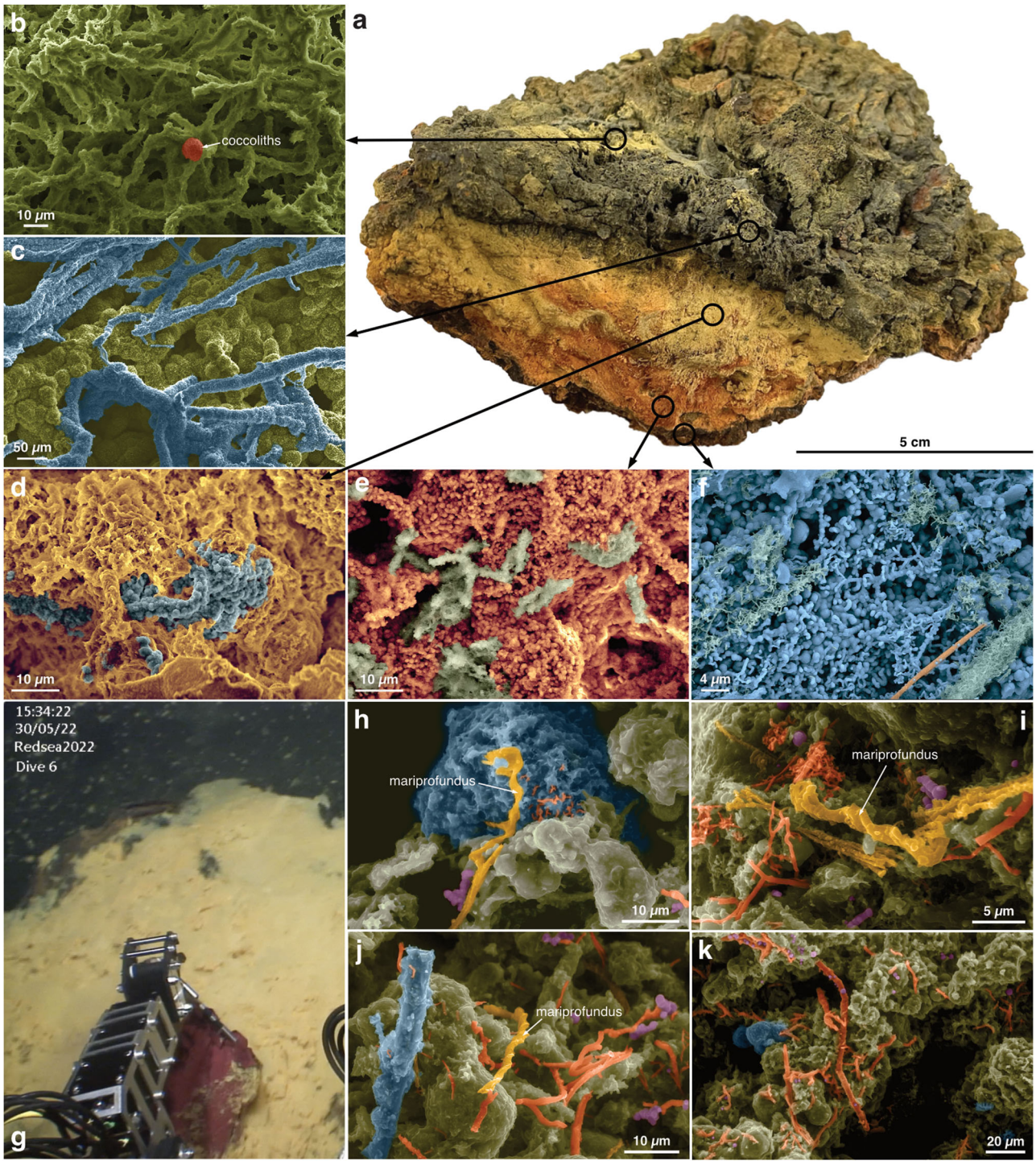

Fig. 4 SEM images of microbial mats and mineralizations in hydrothermal crust. a Fe–Mn crust sampled from Field 8 (sample KRSE4-1 ROV2) with green, yellow, and red layering. The sample is turned upside down, meaning the greenish part was about 10 cm deep inside the mound before sampling. **b**–**f** Colorized SEM images of microbial structures within the Fe–Mn crusts: **b** Network of mineralized bacterial filaments with a scaley, spikey surface (green) and a coccolith shell (red). **c** Denser aggregation of mineralized bacterial spheroids (green) and stalks (blue). **d** Bacterial spheroids (blue) in a denser, irregular sheeted matrix of Fe-oxyhydroxides. **e** Microbial filaments (green) in a dense matrix of small Fe-oxyhydroxide spheroids. **f** Fine microbial network (green) in a course network of the botryoidal and spheroidal matrix. Note that the chosen colors only visually enhance the images' structures and do not represent real colors or specific microbes or minerals. **g** Screengrab from the sampling of a microbial mat within the Farwah Safraa ridges during ROV dive 6. **h**–**k** Colorized SEM images showing characteristic stalks of *Mariprofundus* (yellow in **h**, **i** and **j**) in microbial mat samples.

mats and hydrothermal vents can be categorized into four types based on their morphological appearance (Fig. 3): Type 1 is characterized by focused flow through irregular dm-sized chimneys (1A) or elevated bowl-like structures (1B) with microbial mats at the vent outlets; Type 2 vents include wider, dm to m-sized areas of diffuse flow, occurring mainly at the sides or tops of the mounds. They are covered by voluminous, furry, and fluffy microbial mats (2A) or thinner microbial mats (2B); Type 3

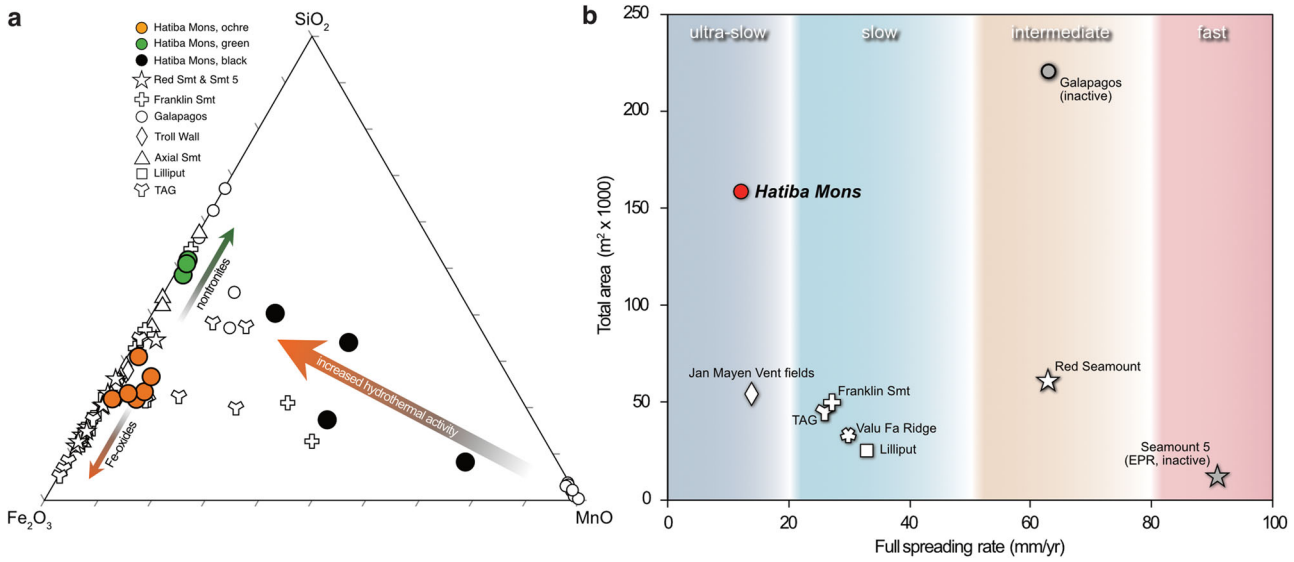

Fig. 5 Comparison of Hatiba Mons to other mid-ocean ridge vent sites. a Ternary diagram of Fe_2O_3, SiO_2, and MnO chemistry of low-T hydrothermal precipitates—Hatiba Mons samples (colored symbols) show a similar large spread as other mid-ocean ridges (white symbols), related to the color of the samples. **b** Total area of hydrothermal occurrences including low-T and high-T (if present) precipitates at mid-ocean ridges with varying spreading rates. Hatiba Mons is in red, active vent fields are in white, and inactive sites are in grey. See also Supplementary Table 3.

occurs in areas of diffuse flow between the mounds and is characterized by white to orange, fluffy microbial heaps (3A) or discolored patches or rings of microbes (3B); Type 4 consists of ovoids or rolls of microbes between mounds and may be accumulated remnants of active microbial communities from higher up. Most types occur at all vent fields, but types 1A and 2A are particularly abundant at *Farwah Safraa* ridges, whereas *Baja'ah Mounds* are characterized by type 1B (Supplementary Table 4).

The sequencing analyses for 16 S rRNA genes from different hydrothermal fields (38 subsamples, Supplementary Tables 1 and 5) revealed a total of 72 prokaryotic phyla (Archaea and Bacteria), with Bacteria being more abundant (Fig. 6). Proteobacteria followed by Chloroflexi and Planctomycetota were the dominant bacterial phyla in the Hatiba hydrothermal fields, while the archaeal community was dominated by Crenarchaeota, Nanoarchaeota, Hydrothermarchaeota, and Thermoplasmatota (Fig. 6). Many of the observed microorganisms are known for performing nitrate-reducing Fe(II)-oxidation, Mn(II)-oxidation and anaerobic oxidation of methane[60,61]. Although not the most abundant, Zetaproteobacteria (an autotrophic iron oxidizer), which are dominated by the genus *Mariprofundus*, were highly prevalent across the microbial mat sample. In addition, microbial groups such as the class Anaerolineae and the phyla DTB120, previously described to be strongly associated with microbial iron mats in other hydrothermal systems, were also detected[62–65] (Fig. 5). Interestingly, anaerobic families, ammonia-oxidizing archaea (e.g., Nitrosopumilales; Fig. 6), and various thermophilic Bacteria and Archaea were also observed, e.g., Rhodothermia that grow at 55–70 °C[66] (Supplementary Fig. 6).

Macrofauna observed at or near the hydrothermal vent fields was sparse and consisted of typical Red Sea deep water species (Fig. 7). The organisms observed from ROV videos include brittle stars, *Ophiocirce* sp. (Ophioleucidae), caridean shrimps, *Plesionika* sp. (Pandalidae, reported from depths around 1000 m[67]), deep-sea squids, *Onykia* sp. (Onychoteuthidae), and teleost fishes comprising congrid eels, *Rhynchoconger* sp. or *Bathycongrus* sp. (Congridae) cusk eels, *Neobythites* sp. (Ophidiidae), and deep-water cods, *Physiculus* sp. (Moridae). Several large-sized *Plesionika* were observed walking or scavenging close to bacterial mats and, at least on one occasion, feeding on bacteria or other organic matter within the mat. Lantern fishes (Myctophidae), barracudinas, *Lestrolepis luxiocula* (Paralepididae), and benthopelagic crustaceans (Lophogastrida and/or Euphausiacea) were frequently seen in the water column 1–3 m above the bottom. The bigeye hound-shark, *Iago omanensis* (Triakidae), was observed in non-hydrothermally active areas.

Volcano-tectonic setting and hydrothermal cooling of Hatiba Mons volcano. Hydrothermal Fe-crusts and mounds are common around seafloor hydrothermal systems at mid-ocean ridges globally. Hydrothermal vents at Hatiba Mons are comparable to those, not only in the chemical compositions of the precipitates (Fig. 5a) but also in the microbial groups that are present[68–70]. However, the Fe-mound fields on Hatiba Mons represent one of the largest known actively forming hydrothermal Fe-accumulations reported from mid-ocean ridges[71–74] (Fig. 5b, Supplementary Table 3). Large hydrothermal sulfide deposits have been previously reported from (ultra)slow-spreading ridges, particularly at magmatic centers or along low-angle detachment faults[37]. Indeed, Hatiba Mons is the largest magmatic center in the ultraslow-spreading Red Sea Rift and a focal point of magmatism[14]. Nevertheless, Hatiba Mons hydrothermal fields comprise an area at least 3× larger than any active vent fields at other ultra-slow to fast-spreading mid-ocean ridges (Fig. 5b; Supplementary Table 3 and references therein). Large Fe-mounds have only been documented from the inactive Galapagos Mounds Abyssal Hydrothermal Field[73]. Hatiba Mons hydrothermal activity is not restricted to particular structures or areas and is instead widespread around the summit, covering large parts of the volcano's surface (Fig. 2). The large number of active vent fields discovered at Hatiba Mons and their widespread distribution contrasts with other hydrothermal sites at (ultra)slow-spreading ridges, where active vent fields are less abundant[75,76] (Fig. 5b, Supplementary Table 3). Extensive, continuously active hydrothermalism and high hydrothermal Fe flux are typically considered to be associated with settings of high magma supply and/or high heat flux, such as fast-spreading ridges[28,77] or during Archaean times[78,79] because of higher lithospheric heat loss due to hydrothermal circulation[80]. Despite being an ultraslow-spreading ridge, a high benthic heat flux

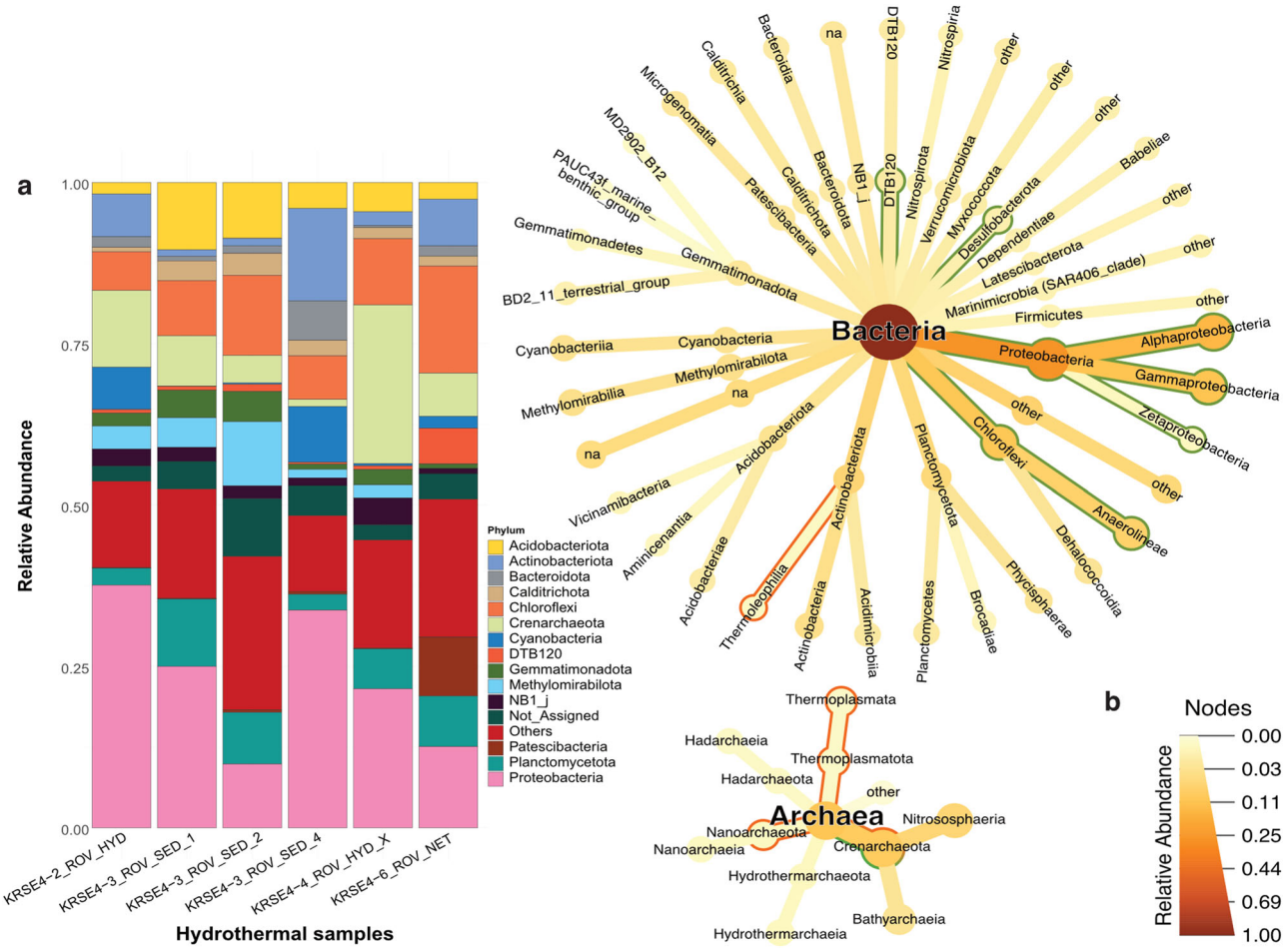

Fig. 6 The relative abundance of prokaryotes found in the Hatiba hydrothermal fields. a Bacteria and Archaea relative abundance from six samples from the Hatiba hydrothermal fields. **b** Dendrogram showing the relative abundance of the overall community of the bacterial and archaeal phyla and classes found in the Hatiba hydrothermal fields. Fe-precipitating groups are highlighted in green, and thermophilic groups are highlighted in orange.

occurs in the Red Sea[35,cf81]. Additionally, abundant volcanic edifices and the lack of ultramafic rocks at the seafloor[14] point to unusually high magmatic activity along the entire Red Sea Rift, which is interpreted to be related to the Afar plume[10] and/or the isolating effect of the former continent[82]. Therefore, abundant widespread hydrothermal activity at Hatiba Mons could be the result of enhanced Red Sea heat flow. Alternative possibilities to explain the widespread low-T venting are (1) the presence of a high ductile (hot) crust beneath Hatiba Mons as indicated by the low seismicity in the area and the hourglass-shaped fault pattern[53,83], or (2) extensive faulting of the volcano itself. A ductile crust could prevent the formation of a deep high-T hydrothermal circulation cell. This process has been invoked, for instance, for the Lilliput Field, a low-T vent site at the southern Mid-Atlantic Ridge[72], which is closely related to the cooling of a recent dike intrusion and associated young lava fields. In contrast, the active mounds at Hatiba Mons are not related to young lava flows (Fig. 2). Here, the elevated trace element concentrations in the hydrothermal precipitates indicate a deep-seated hydrothermal convection cell as suggested for metalliferous precipitates elsewhere[59]. Therefore, extensive faulting of the volcano is the more likely cause of the high abundance of low-T vent sites. An extensive fault density at Hatiba Mons is particularly apparent when compared to areas with known high-T venting, such as the TAG hydrothermal field[74] and Axial Seamount[84] (both mapped by AUV at the same resolution as this study; Supplementary Fig. 3). Hatiba Mons has both, a higher average fault density ($>1 \times 10^{-2}$ m/m^2 vs. $<<1 \times 10^{-2}$ m/m^2), and a larger area of the volcano summit that is strongly faulted (50% with $>1 \times 10^{-2}$ m/m^2; Supplementary Fig. 3). This high fault density combined with Hatiba Mons' positive relief could provide easy entrance for seawater into the volcano, leading to effective cooling of the upper parts. This may explain the diffuse low-T venting of hydrothermal fluids along numerous pathways, with the possibility of high-T mineralization deeper in the system.

The studied mound fields at Hatiba Mons are all very similar in terms of their geological setting, morphology, mineralogy, chemistry and microbial communities. Variations in hydrothermal crust chemistry can be explained by local variations in fluid chemistry and or activity of the venting, e.g., Johannessen et al.[71] showed that Mn-oxides are formed during phases of low hydrothermal activity, while Fe-oxides are formed during phases of high activity (Fig. 5a). Local variations in abundance of microbial mats are unrelated to their location on the summit. Low abundances of microbial mats, however, seem to be associated with a lower mound relief and are most likely related to limited hydrothermal activity (e.g., central *Kabir Field*; Fig. 2f). The only systematic variation between the fields is that the mounds associated with the large fault systems on the W- and NE-platforms appear to be higher, more solid, and consisting of higher amounts of black Mn-oxides, rather than the softer reddish Fe-oxides in the central valley. Additionally, the Farwah Safraa ridges display more focused (type 1A) venting than the

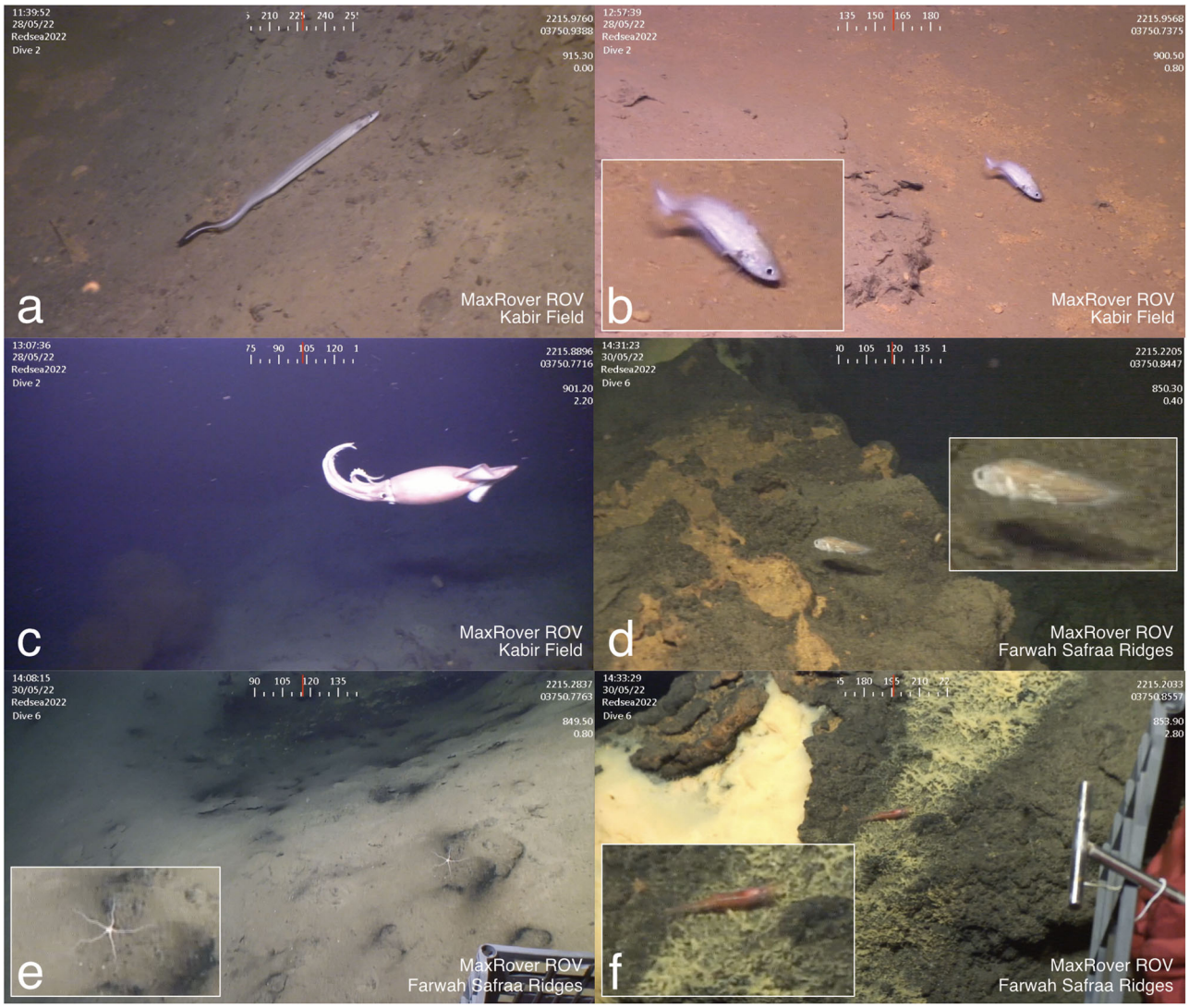

Fig. 7 Macrofauna observed near the Hatiba Mons hydrothermal mounds. a Congrid eel, probably *Rhynchoconger* sp. or *Bathycongrus* sp. (Congridae). **b** Deep-water cod, *Physiculus* sp., possibly *P. marisrubri* (Moridae). **c** Deep-sea squid, probably *Onykia* sp. (Onychoteuthidae). **d** Cusk eel, possibly *Neobythites* sp. (Ophidiidae). **e** Ophiuroid, *Ophiocirce* sp., possibly *O. seminudum* (Ophioleucidae). **f** Caridean shrimp, *Plesionika* sp. (Pandalidae), scavenging close to bacterial mats. ROV images were taken with the MaxRover ROV from HCMR, Athens.

other areas, likely related to the presence of larger bounding faults that may reach deeper and focus venting.

Genesis of large hydrothermal mounds and the role of biological activity. Fe-oxyhydroxide mounds formed by low-T hydrothermal venting and associated microbial communities are found in many locations worldwide[68,69,71]. However, it is still debated whether Fe-mounds are predominantly formed by biogenic or authigenic processes, such as low-T precipitation or the weathering of high-T sulfide precipitates[69,71,85]. The weathering of high-T minerals can be excluded at Hatiba Mons because of the observed textures, the chemical composition (e.g., low S and Cu), and the lack of relict sulfides in hand specimens and XRD data. SEM imaging of the Mn-oxides, and some Fe-oxides, shows evidence of some authigenic precipitation. Nevertheless, the majority of our samples indicate the importance of microbial-induced mineralization, as suggested by the high abundance of organic textures and structures observed under SEM and optical microscope (Fig. 4). Members of the class Zetaproteobacteria commonly shape the structure of microbial mats in high-Fe environments, such as diffuse hydrothermal vents[86]. Recent studies have shown that the activity of, e.g., *Zetaproteobacteria* at Kama'ehuakanaloa[87], the Jan Mayen Vent Fields[71], and Iwo-Jima Island[88] play a major role in Fe-oxide deposition. The autotrophic Fe(II)-oxidizing Zetaproteobacteria observed at Hatiba Mons are microaerophilic, which confers a competitive advantage over merely authigenic Fe(II)-oxidation at the oxic/anoxic transition[65]. Additionally, groups like Calditrichota, Gemmatimonadota, Hydrogenedentota, Nitrospinota, Planctomycetota, Acidobacteriota, Gammaproteobacteria, and Bacteroidota were found. Also, these microbial groups were predicted to play a role in Fe-cycling based on metagenomic analysis, e.g., from Longqi hydrothermal vents, Southwest Indian Ridge[70]. Fe(II)-oxidizing groups[65,89,90] are most common at Hatiba Mons in microbial mats but are also detected in crusts and sediments (Fig. 5). Thus, we suggest that microbial activity plays a major role in the formation of the hydrothermal mounds at Hatiba Mons. In-depth analysis of the functional capabilities of samples from Hatiba is, however, needed to understand the exact roles of the diverse prokaryotes in mineral cycles in the Red Sea's hydrothermal vents.

However, the reason for such widespread microbial activity and why the mounds are notably larger at Hatiba Mons than

comparable sites at other mid-ocean ridges (Supplementary Table 3)[71,87,88] remains unknown. The microbes could be specialized to the Red Sea conditions and have advantages that make them more versatile. This is, however, not directly evident from the groups present, which are similar to other mid-ocean ridges[68–70] (Fig. 6). Further functional and targeted studies, such as the use of models based on metagenomics, meta-transcriptomics, and isolating different microorganisms are necessary to validate or refute this hypothesis. One alternative reason may be the absence of grazing by (specialized) heterotrophic vent fauna feeding on the mound-building microbes and/or chemosynthetic communities competing for nutrients from the fluids. Diverse and specialized chemosynthetic benthic metazoan communities with high endemism and strong zonation patterns are known globally from most deep-sea hydrothermal vent fields[91–93]. Notably, however, specialized deep vent fauna is absent at Hatiba Mons; there could be multiple explanations for this. First, specialized vent fauna could be present within our study site at, so far undiscovered high-T vent sites. Sulfide oxidation is generally associated with high-T hydrothermal vents and promotes symbiosis with the vent fauna[94]. The absence of sulfide-oxidizing bacteria may be an explanation for the lack of symbionts in low-T Hatiba vents. On the contrary, low-T hydrothermal vents are characterized by Fe-oxidizing microbial metabolism by abundant Fe(III)-rich microbial mats[95,96]. Iron-oxidizing microbes could, therefore, have a competitive advantage over sulfide oxidation in low-T iron-rich sources. However, chemosymbiotic vent communities are not exclusive to high-T vent fields and also occur on low-T Fe-mounds, e.g., in the Atlantic[72]. A second possible explanation could be unfavorable environmental conditions for metazoans. The observations of common deep benthic organisms at Hatiba Mons (Fig. 7), however, suggest its vent field environment is hospitable for metazoan life. The presence of specialized vent fauna on Fe-mounds worldwide also indicates that this substrate is, in general, a suitable habitat[71,72]. However, the combination of warm and highly saline seawater in the deep Red Sea and potentially unfavorable hydrothermal fluid chemistry related to the low temperatures could be a limiting factor for symbiont-hosting macrofauna (e.g., fluids with low CH_4, H_2, H_2S, as indicated by the low S in the hydrothermal precipitates; Supplementary Table 2). Third, oceanographic (e.g., seasonal high salinity deep water outflows into the Gulf of Aden[97]) and physical barriers (i.e., the narrow and shallow entrance to the Red Sea[98]) lead to geographic isolation and limit dispersal, colonization, and connectivity of vent fauna from the adjacent Gulf of Aden into the deep Red Sea. Finally, the relatively short and dynamic evolution of the Red Sea itself[10], with the latest extinction event ~20,000 years ago, may have limited the evolutionary history of hydrothermal fauna. Additional exploration and environmental data collection could test the suitability of the deep Red Sea for specialized vent fauna.

In conclusion, we located active hydrothermal venting in the Red Sea for the first time. The active fields of low-T Fe-oxyhydroxides at Hatiba Mons, associated with abundant, thriving microbial communities, are larger than those known from any other (ultra)slow-spreading ridge so far. This appears to be related to a combination of (1) effective cooling of the Hatiba Mons volcano due to high fault densities, resulting in widespread diffuse venting of low-T fluids, and (2) the absence of vent-specific macrofauna and, therefore, limited grazing pressure and no competition for nutrients. The flourishing microbial communities, in turn, provide the opportunity to build, over time, the large mounds observed at Hatiba Mons. The warm water temperatures may also make the deep Red Sea a candidate for an analog to Precambrian Oceans. These similar environments, together with the presence of large iron deposits and thriving microbes (although genetically not necessarily related), could be particularly relevant to understanding the relationship between early life on Earth and the formation of large iron deposits (Banded Iron Formations) during a time when macrofauna was still absent[52].

Methods

Hydroacoustic mapping, water column data, ROV observations, and temperature measurements. Ship-based tow-yos with five MAPRs (Miniature Autonomous Plume Recorders provided by NOAA) were carried out in the fall of 2021 from the RV Azizi. The MAPRs were evenly spaced 50 m apart, and the water column was scanned along SE-NW directed lines over the summit area of the Hatiba Mons volcano. Due to the lack of availability of a USBL transponder, the exact position of the MAPR along the profiles is unknown. Nevertheless, the water column anomalies were used to identify morphologically attractive targets in AUV multibeam data and narrow the search area for AUV mapping and ROV dives.

High-resolution bathymetry mapping was conducted in February 2022 from the OSS Handin Tide with a 6000 m depth-rated Hugin Superior AUV provided by FUGRO. The AUV carried a Kongsberg EM2040 Mk2 multibeam echosounder, EdgeTech Subbottom profiler, and CTD. The AUV flew at a constant altitude of 90 m in bottom-following mode. The EM2040 was set to 200 kHz, and USBL navigation data were post-processed in NavLab. Bathymetry was post-processed and merged with the corrected navigation in QPS Qimera. Multibeam backscatter was mosaiced in QPS FMGT from the raw data and cleaned GSF exports. AUV turbidity data were processed and averaged in Octave 6.2. All geospatial data were imported in QGIS 3 for further interpretation and to plan the ROV dives. FUGRO ROV (OSS Handin Tide) and ROV MaxRover (RV Aegaeo) dives in February and May 2022 and February 2023 were guided by the 2-m resolution AUV maps. USBL gave a navigation accuracy of <2 m and ~50 m for the different ROVs.

Temperature measurements were performed with an untethered HOBO temperature logger with a range of −40 °C to 125 °C during MaxRover ROV dives in February 2023. Due to rough weather conditions, which reduced ROV stability, the accurate placement of the T-sensor at the vent outlets was difficult and therefore, the T-measurement of pure vent fluids was not possible.

Rock sampling, mineralogy, and geochemistry. Sampling was performed by a mechanical arm with shovels, push cores, and microbial nets. Representative rock samples were dried at 30 °C and pulverized. The bulk rock mineralogy was determined by X-ray diffractometry (XRD) at the Institute for Geosciences, University of Kiel, Germany, using a Bruker AXS D 8 Discover diffractometer with automatic divergence slit, Θ–Θ-geometry and mono-chromatic CoKα radiation (step size 0,037° 2Θ, count interval 1.5 s, angular coverage 10°–70° 2Θ). Processing of the XRD-raw-data was performed using the freeware MacDiff[99].

Major and trace elements were analyzed by ALS Loughrea by combining XRF (LiB fusion) ICP-MS, IR Spectroscopy (S and C), and base metal 4-acid digestion.

Major elements of basalt glasses were measured with a Jeol JXA-8200 “Superprobe” electron microprobe at GEOMAR, Kiel, using an acceleration voltage of 15 kV, a defocused spot of 5 µm diameter, and a beam current of 10 nA. Counting times were 20/10 s (background/peak) for Si, Al, Mg, Ca, P, 10/10 s for Na, 30/15 s for Ti, Fe, K, S, Cl, and 40/20 s for Mn. For calibration and monitoring of data quality, natural reference samples from the

Smithsonian Institute were used[100]. Relative analytical precision and accuracy are generally better than 2.5%, but up to 5% for Na_2O and K_2O, and on average 30% for MnO and P_2O_5, and 50% for Cl and S.

SEM was performed by KAUST imaging and characterization Corelab. Hydrothermal crust samples were mounted on an aluminum stub, coated with 5 nm of platinum, and imaged by a Zeiss Merlin Gemini II using 5, 10, or 15 kV. Microbial samples were imaged with a ThermoFisher Quattro ESEM using a GSED detector under pressure of 1417 Pa and 15 kV.

Microbial sampling. Samples (38 subsamples from crusts, sediments, and microbial mats) were collected in the Red Sea Rift during the KRSE Aegaeo RV cruise in May 2022 (Supplementary Tables 1 and 5). Vent samples from Site 8 and the microbial mats from Farwah Safraa were collected using an ROV hydraulic arm. Sediments and mats were collected from the Kabir Field using push cores. All samples were placed in sterile Whirl-Pak bags and Falcon tubes, immediately stored at −20 °C, and transported to the laboratory in a cooler with ice before permanent storage at −80 °C.

DNA extraction and sequencing. DNA was extracted from each sample (10 g) using a DNeasy PowerMax Soil Kit (Qiagen, Hilden, Germany) following the manufacturer's protocol. DNA concentration and integrity were checked using a Qubit dsDNA HS Assay and Qubit fluorometer 4.0 (ThermoFisher Scientific, Waltham, USA) and agarose gel (1%) electrophoresis, respectively.

Extracted DNA was subjected to sequencing of the prokaryotic communities at MR DNA (Molecular Research LP, Shallowater, USA). DNA was amplified using the universal primer set 515 F (5'-GTGCCAGCMGCCGCGGTAA-3′) and 806 R (5'-GGACTACHVGGGTWTCTAAT-3') covering the V4 region of the 16 S rRNA gene. Additionally, amplification was performed using the HotStarTaq Plus Master Mix Kit (Qiagen, USA), as follows: initial denaturation at 95 °C for 5 min, followed by 30 cycles at 95 °C for 30 s, 53 °C for 40 s, and 72 °C for 1 min, and a final extension step at 72 °C for 10 min. PCR products were run in 2% agarose gel and subsequently used to prepare the barcoded library. Libraries were quantified using a bioanalyzer, normalized, pooled at an equimolar ratio based on their molecular weight and IST concentrations, and purified using AMPure XP beads. Paired-end IST bacterial sequencing (2 × 250 bp) was performed using a NovaSeq 6000 reagent kit (Illumina, USA) according to the standard protocol to produce raw sequence data.

Sequencing data processing. The 16 S rRNA gene amplicon libraries were processed using the DADA2 pipeline[101]. PhiX and adaptors were removed from the raw reads using the BBDuk tool from the BBMap suite (http://sourceforge.net/projects/bbmap/). The Cutadapt tool[102] was used to trim the primers. Forward and reverse sequences were merged to obtain the complete denoised reads. The amplicon sequence variant table (ASV) was created for the 16 S rRNA data, and chimeras were removed. Reads were analyzed using a pseudo-pooling method and taxonomy was assigned using the SILVA reference database, version 138.1[103].

Data analysis. Relative abundance analyses were performed using MicrobiomeAnalyst 2.0 (https://www.microbiomeanalyst.ca). Contaminants are removed by applying the low counts and low variance filter using the default parameters. Data are rarefied to the minimum library size and normalized by the total sum scaling. The relative abundance results from MicrobiomeAnalyst 2.0 are visualized in Metacoder[104] and ggplot2[105] in R environment[106].

Reporting summary. Further information on research design is available in the Nature Portfolio Reporting Summary linked to this article.

Data availability

The 2 m gridded bathymetry and backscatter mosaics are available from the Pangaea data repository (https://doi.org/10.1594/PANGAEA.956871). The microbiological data generated in this study are available in the National Center for Biotechnology Information (NCBI) database under the BioProject ID PRJNA910929 under the accession numbers SAMN32151258 – SAMN32151298 (see Supplementary Table 5). Geochemical data, ROV data, and AUV raw data may be requested from the corresponding author.

Received: 22 March 2023; Accepted: 7 December 2023;
Published online: 21 December 2023

References

1. German, C., Baker, E. & Klinkhammer, G. Regional setting of hydrothermal activity. *Geol. Soc. Lond. Spec. Publ.* **87**, 3–15 (1995).
2. Hannington, M. D., de Ronde, C. D. & Petersen, S. in *Economic Geology 100th Anniversary Volume*. 111–141 (Society of Economic Geologists, 2005).
3. Menini, E. & Van Dover, C. L. An atlas of protected hydrothermal vents. *Mar. Policy* **108**, 103654 (2019).
4. Corliss, J. B. et al. Submarine thermal springs on the Galapagos Rift. *Science* **203**, 1073–1083 (1979).
5. Schopf, J. W. *Earth's Earliest Biosphere: Its Origin and Evolution*. (1983).
6. Russell, M. & Hall, A. The emergence of life from iron monosulphide bubbles at a hydrothermal redox front. *J. Geol. Soc.* **154**, 377–402 (1996).
7. Macleod, G., McKeown, C., Hall, A. J. & Russell, M. J. Hydrothermal and oceanic pH conditions of possible relevance to the origin of life. *Orig. Life Evolut. Biosph.* **24**, 19–41 (1994).
8. Pace, N. R. A molecular view of microbial diversity and the biosphere. *Science* **276**, 734–740 (1997).
9. Van Dover, C. L., German, C., Speer, K. G., Parson, L. & Vrijenhoek, R. Evolution and biogeography of deep-sea vent and seep invertebrates. *Science* **295**, 1253–1257 (2002).
10. Augustin, N., van der Zwan, F. M., Devey, C. W. & Brandsdóttir, B. 13 million years of seafloor spreading throughout the Red Sea Basin. *Nat. Commun.* **12**, 2427 https://doi.org/10.1038/s41467-021-22586-2 (2021).
11. Delaunay, A. et al. Structure and morphology of the Red Sea, from the mid-ocean ridge to the ocean-continent boundary. *Tectonophysics* https://doi.org/10.1016/j.tecto.2023.229728 (2023).
12. Mitchell, N. C., Ligi, M., Ferrante, V., Bonatti, E. & Rutter, E. Submarine salt flows in the central Red Sea. *Geol. Soc. Am. Bull.* **122**, 701–713 (2010).
13. Augustin, N. et al. The rifting to spreading transition in the Red Sea. *Earth Planet. Sci. Lett.* **395**, 217–230 (2014).
14. Augustin, N. et al. Geomorphology of the central Red Sea Rift: determining spreading processes. *Geomorphology* **274**, 162–179 (2016).
15. Cochran, J. R. A model for development of Red Sea. *AAPG Bull.* **67**, 41–69 (1983).
16. Roeser, H. A. A detailed magnetic survey of the southern Red Sea. *Geologisches Jahrb.* **13**, 131–153 (1975).
17. Pautot, G. Les fosses de la Mer Rouge: approche géomorphologique d'un stade initial d'ouverture océanique réalisée à l'aide du Seabeam. *Oceanol. Acta* **6**, 235–244 (1983).
18. Bonatti, E. Punctiform initiation of seafloor spreading in the Red Sea during transition from a continental to an oceanic rift. *Nature* **316**, 33–37 (1985).
19. Feldens, P. & Mitchell, N. C. in *The Red Sea* (eds Najeeb M. A.Rasul & Ian C. F.Stewart) 205–218 (Springer, 2015).
20. Miller, A. R. et al. Hot brines and recent iron deposits in deeps of the Red Sea. *Geochim. Cosmochim. Acta* **30**, 341–359 (1966).
21. Swallow, J. C. & Crease, J. Hot salty water at the bottom of the Red Sea. *Nature* **205**, 165–166 (1965).
22. Schmidt, M., Al-Farawati, R. & Botz, R. in *The Red Sea* (eds Najeeb M. A.Rasul & Ian C. F.Stewart) 219–233 (Springer, 2015).
23. Bäcker, H. & Richter, H. Die rezente hydrothermal-sedimentäre Lagerstätte Atlantis-II-Tief im Roten Meer. *Geologische Rundsch.* **62**, 697–737 (1973).

24. Gurvich, E. G. in *Metalliferous Sediments of the World Ocean: Fundamental Theory of Deep-Sea Hydrothermal Sedimentation* 127–210 (Springer Berlin Heidelberg, 2006).
25. Blum, N. & Puchelt, H. Sedimentary-hosted polymetallic massive sulfide deposits of the Kebrit and Shaban Deeps, Red Sea. *Miner. Depos.* **26**, 217–227 (1991).
26. Monin, A. et al. Red sea submersible research expedition. *Deep Sea Res. Part A* **29**, 361–373 (1982).
27. Beaulieu, S. E., Baker, E. T. & German, C. R. Where are the undiscovered hydrothermal vents on oceanic spreading ridges? *Deep Sea Res. Part II* **121**, 202–212 (2015).
28. Michael, P. J. & Cornell, W. C. Influence of spreading rate and magma supply on crystallization and assimilation beneath mid-ocean ridges: evidence from chlorine and major element chemistry of mid-ocean ridge basalts. *J. Geophys. Res.* **103**, 18325–18356 (1998).
29. Coogan, L. A., Mitchell, N. C. & O'Hara, M. J. Roof assimilation at fast spreading ridges: an investigation combining geophysical, geochemical, and field evidence. *J. Geophys. Res.* **108**, 2–14 (2003). ECV 2-1-ECV.
30. van der Zwan, F. M. et al. Lower crustal hydrothermal circulation at slow-spreading ridges: evidence from chlorine in Arctic and South Atlantic basalt glasses and melt inclusions. *Contrib. Mineral. Petrol.* **172**, 97 (2017).
31. van der Zwan, F. M. et al. Hydrothermal activity at the ultraslow- to slow-spreading Red Sea Rift traced by chlorine in basalt. *Chem. Geol.* **405**, 63–81 (2015).
32. van der Zwan, F. M., Devey, C. W. & Augustin, N. Hydrothermal Prospection in the Red Sea Rift: Geochemical messages from Basalts. in *Geological Setting, Palaeoenvironment and Archaeology of the Red Sea* (eds Najeeb M. A. Rasul & Ian C. F. Stewart) 221–232 (Springer International Publishing, 2019).
33. Chu, D. & Gordon, R. G. Current plate motions across the Red Sea. *Geophys. J. Int.* **135**, 313–328 (1998).
34. ArRajehi, A. et al. Geodetic constraints on present-day motion of the Arabian Plate: implications for Red Sea and Gulf of Aden rifting. *Tectonics* **29** (2010).
35. Girdler, R. W. & Evans, T. R. Red Sea heat flow. *Geophys. J. Int.* **51**, 245–251 (1977).
36. Fouquet, Y. Where are the large hydrothermal sulphide deposits in the oceans? *Philos. Trans. R. Soc. Lond. Ser. A* **355**, 427–441 (1997).
37. German, C. R., Petersen, S. & Hannington, M. D. Hydrothermal exploration of mid-ocean ridges: where might the largest sulfide deposits be forming? *Chem. Geol.* **420**, 114–126 (2016).
38. Guney, M., Al-Marhoun, M. A. & Nawab, Z. A. Metalliferous sub-marine sediments of the Atlantis-II-Deep, Red Sea. *Can. Min. Met. Bull.* **81**, 33–39 (1988).
39. Laurila, T. E., Hannington, M. D., Petersen, S. & Garbe-Schönberg, D. Early depositional history of metalliferous sediments in the Atlantis II deep of the Red Sea: evidence from rare earth element geochemistry. *Geochim. Cosmochim. Acta* **126**, 146–168 (2014).
40. Pearse, A. & Gunter, G. *Salinity*. (1957).
41. Yao, F. & Hoteit, I. Rapid Red Sea deep water renewals caused by volcanic eruptions and the north Atlantic oscillation. *Sci. Adv.* **4**, eaar5637 (2018).
42. Berumen, M. L. et al. *The Red Sea: Environmental Gradients Shape a Natural Laboratory in A Nascent Ocean*. (Springer, 2019).
43. Cann, J., Winter, C. & Pritchard, R. A hydrothermal deposit from the floor of the Gulf of Aden. *Mineral. Mag.* **41**, 193–199 (1977).
44. Choukroune, C. S. T. et al. Tectonics of the westernmost Gulf of Aden and the Gulf of Tadjoura from submersible observations. *Nature* **319**, 396–399 (1986).
45. Juniper, S. K., Tunnicliffe, V. & Desbruyères, D. in *Gorda Ridge* 265–278 (Springer, 1990).
46. Zajonz, U., Cheung, C. & DeVantier, L. Deep-dwelling fish fauna of the Gulf of Aden and Red Sea. *Socotra. A Natural History of the Islands and Their People*. (Odyssey Books and Guides, Hong Kong, 2007).
47. Taviani, M. Post-Miocene reef faunas of the Red Sea: glacio-eustatic controls. *Sedimentation and Tectonics in Rift Basins Red Sea:-Gulf of Aden*, 574–582 (1998).
48. DiBattista, J. D. et al. A review of contemporary patterns of endemism for shallow water reef fauna in the Red Sea. *J. Biogeogr.* **43**, 423–439 (2016).
49. Knauth, L. P. in *Geobiology: Objectives, Concepts, Perspectives* 53–69 (Elsevier, 2005).
50. Saito, T. et al. PIXE and microthermometric analyses of fluid inclusions in hydrothermal quartz from the 2.2 Ga Ongeluk Formation, South Africa: implications for ancient seawater salinity. *Precambrian Res.* **286**, 337–351 (2016).
51. Tartèse, R., Chaussidon, M., Gurenko, A., Delarue, F. & Robert, F. Warm Archean oceans reconstructed from oxygen isotope composition of early-life remnants. *Geochem. Perspect. Lett.* **3**, 55–65 (2017).
52. Konhauser, K. O. *Hydrothermal Bacterial Biomineralization: Potential Modern-Dayanalogues Forbandediron-Formations*. (2000).
53. Merle, O. & Borgia, A. Scaled experiments of volcanic spreading. *J. Geophys. Res.* **101**, 13805–13817 (1996).
54. Centre, I. S. *On-line Bulletin*. http://www.isc.ac.uk (2011).
55. Ligi, M. et al. Birth of an ocean in the Red Sea: Initial pangs. *Geochem. Geophys. Geosyst.* **13**, Q08009 (2012).
56. Szitkar, F., Dyment, J., Choi, Y. & Fouquet, Y. What causes low magnetization at basalt-hosted hydrothermal sites? Insights from inactive site Krasnov (MAR 16° 38′ N). *Geochem. Geophys. Geosyst.* **15**, 1441–1451 (2014).
57. Kashefi, K. & Lovley, D. R. Extending the upper temperature limit for life. *Science* **301**, 934–934 (2003).
58. Blount, C. & Dickson, F. The solubility of anhydrite (CaSO) in NaC1-H• O from 100 ø to 450 ø C and 1 to 1,000 bars. *Geochim. Cosmochim. Acta* **33**, 227–245 (1969).
59. Mills, R. A. & Elderfield, H. Hydrothermal activity and the geochemistry of metalliferous sediment. *Geophys. Monogr.* **91**, 392–392 (1995).
60. Handley, K. M. & Lloyd, J. R. Biogeochemical implications of the ubiquitous colonization of marine habitats and redox gradients by Marinobacter species. *Front. Microbiol.* **4**, 136 (2013).
61. Jiang, L. et al. Characterization of anaerobic oxidation of methane and microbial community in landfills with aeration. *Environ. Res.* **214**, 114102 (2022).
62. Nunoura, T. et al. Isolation and characterization of a thermophilic, obligately anaerobic and heterotrophic marine Chloroflexi bacterium from a Chloroflexi-dominated microbial community associated with a Japanese shallow hydrothermal system, and proposal for Thermomarinilinea lacunofontalis gen. nov., sp. nov. *Microbes Environ.* **28**, 228–235 (2013).
63. Hoshino, T. et al. Ecophysiology of Zetaproteobacteria associated with shallow hydrothermal iron-oxyhydroxide deposits in Nagahama Bay of Satsuma Iwo-Jima, Japan. *Front. Microbiol.* **6**, 1554 (2016).
64. Pop Ristova, P., Pichler, T., Friedrich, M. W. & Bühring, S. I. Bacterial diversity and biogeochemistry of two marine shallow-water hydrothermal systems off Dominica (Lesser Antilles). *Front. Microbiol.* **8**, 2400 (2017).
65. McAllister, S. M., Vandzura, R., Keffer, J. L., Polson, S. W. & Chan, C. S. Aerobic and anaerobic iron oxidizers together drive denitrification and carbon cycling at marine iron-rich hydrothermal vents. *ISME J.* **15**, 1271–1286 (2021).
66. Hahnke, R. L. et al. Genome-based taxonomic classification of Bacteroidetes. *Front. Microbiol.* **7**, 2003 (2016).
67. Fransen, C. Pandalidae (Crustacea: Decapoda) of the SONNE, VALDIVIA and METEOR Expeditions 1977–1987 to the Red Sea and the Gulf of Aden. *Senckenbergiana Marit.* **36**, 51–82 (2006).
68. Kennedy, C., Scott, S. & Ferris, F. Characterization of bacteriogenic iron oxide deposits from Axial Volcano, Juan de Fuca Ridge, northeast Pacific Ocean. *Geomicrobiol. J.* **20**, 199–214 (2003).
69. Boyd, T. & Scott, S. Microbial and hydrothermal aspects of ferric oxyhydroxides and ferrosic hydroxides: the example of Franklin Seamount, Western Woodlark Basin, Papua New Guinea. *Geochem. Trans.* **2**, 45–56 (2001).
70. Zhong, Y.-W. et al. Metagenomic features characterized with microbial iron oxidoreduction and mineral interaction in southwest Indian ridge. *Microbiol. Spectr.* **10**, e00614–e00622 (2022).
71. Johannessen, K. C. et al. Environmental controls on biomineralization and Fe-mound formation in a low-temperature hydrothermal system at the Jan Mayen Vent Fields. *Geochim. Cosmochim. Acta* **202**, 101–123 (2017).
72. Haase, K. et al. Diking, young volcanism and diffuse hydrothermal activity on the southern Mid-Atlantic Ridge: The Lilliput field at 9 33′S. *Mar. Geol.* **266**, 52–64 (2009).
73. Lonsdale, P. Deep-tow observations at the mounds abyssal hydrothermal field, Galapagos Rift. *Earth Planet. Sci. Lett.* **36**, 92–110 (1977).
74. Graber, S. et al. Structural control, evolution, and accumulation rates of massive sulfides in the TAG hydrothermal field. *Geochem. Geophys. Geosyst.* **21**, e2020GC009185 (2020).
75. Marcon, Y. et al. Megafaunal distribution and assessment of total methane and sulfide consumption by mussel beds at Menez Gwen hydrothermal vent, based on geo-referenced photomosaics. *Deep Sea Res. Part I* **75**, 93–109 (2013).
76. German, C. R. et al. Volcanically hosted venting with indications of ultramafic influence at Aurora hydrothermal field on Gakkel Ridge. *Nat. Commun.* **13**, 1–11 (2022).
77. Hannington, M., Jamieson, J., Monecke, T., Petersen, S. & Beaulieu, S. The abundance of seafloor massive sulfide deposits. *Geology* **39**, 1155–1158 (2011).
78. Isley, A. E. Hydrothermal plumes and the delivery of iron to banded iron formation. *J. Geol.* **103**, 169–185 (1995).
79. Lowell, R. P. & Keller, S. M. High-temperature seafloor hydrothermal circulation over geologic time and archean banded iron formations. *Geophys. Res. Lett.* **30** (2003).
80. Stein, C. A., Stein, S. & Pelayo, A. M. in *Seafloor Hydrothermal Systems: Physical, Chemical, Biological, and Geological Interactions* 425–445 (American Geophysical Union, 2013).
81. Fuchs, S. et al. The global heat flow database: Release 2021. (2021).

82. Brandl, P. A., Regelous, M., Beier, C. & Haase, K. M. High mantle temperatures following rifting caused by continental insulation. *Nat. Geosci.* **6**, 391 (2013).
83. van Wyk de Vries, B. & Merle, O. The effect of volcanic constructs on rift fault patterns. *Geology* **24**, 643–646 (1996).
84. Clague, D. A. et al. Preliminary 1-meter resolution bathymetric model (ESRI ASCII grids) for the summit region of Axial Seamount, version as of 10 March 2021. *IEDA Marine Geoscience Datasystem* https://doi.org/10.26022/IEDA/330219 (2022).
85. Ta, K. et al. Hydrothermal nontronite formation associated with microbes from low-temperature diffuse hydrothermal vents at the South Mid-Atlantic Ridge. *J. Geophys. Res.* **122**, 2375–2392 (2017).
86. Fullerton, H., Hager, K. W., McAllister, S. M. & Moyer, C. L. Hidden diversity revealed by genome-resolved metagenomics of iron-oxidizing microbial mats from Lō'ihi Seamount, Hawai'i. *ISME J.* **11**, 1900–1914 (2017).
87. Edwards, K. J. et al. Ultra-diffuse hydrothermal venting supports Fe-oxidizing bacteria and massive umber deposition at 5000 m off Hawaii. *ISME J.* **5**, 1748–1758 (2011).
88. Kiyokawa, S., Kuratomi, T., Hoshino, T., Goto, S. & Ikehara, M. Hydrothermal formation of iron-oxyhydroxide chimney mounds in a shallow semi-enclosed bay at Satsuma Iwo-Jima Island, Kagoshima, Japan. *GSA Bull.* **133**, 1890–1908 (2021).
89. McAllister, S. M. et al. Validating the Cyc2 neutrophilic Fe oxidation pathway using meta-omics of Zetaproteobacteria iron mats at marine hydrothermal vents. *bioRxiv,* 722066 https://doi.org/10.1128/msystems.00553-19 (2019).
90. Emerson, D. et al. A novel lineage of proteobacteria involved in formation of marine Fe-oxidizing microbial mat communities. *PloS ONE* **2**, e667 (2007).
91. Copley, J. T. et al. Ecology and biogeography of megafauna and macrofauna at the first known deep-sea hydrothermal vents on the ultraslow-spreading Southwest Indian Ridge. *Sci. Rep.* **6**, 1–13 (2016).
92. Sarrazin, J. et al. Biodiversity patterns, environmental drivers and indicator species on a high-temperature hydrothermal edifice, Mid-Atlantic Ridge. *Deep Sea Res. Part II* **121**, 177–192 (2015).
93. Perez, M., Sun, J., Xu, Q. & Qian, P.-Y. Structure and connectivity of hydrothermal vent communities along the mid-ocean ridges in the west Indian. *Oceanology* **8**, 744874 (2021).
94. Georgieva, M. N. et al. Sulfur isotopes of hydrothermal vent fossils and insights into microbial sulfur cycling within a lower Paleozoic (Ordovician-early Silurian) vent community. *Geobiology* **20**, 465–478 (2022).
95. Emerson, D., Fleming, E. J. & McBeth, J. M. Iron-oxidizing bacteria: an environmental and genomic perspective. *Annu. Rev. Microbiol.* **64**, 561–583 (2010).
96. Templeton, A. S. Geomicrobiology of iron in extreme environments. *Elements* **7**, 95–100 (2011).
97. Bower, A. S., Fratantoni, D. M., Johns, W. E. & Peters, H. Gulf of Aden eddies and their impact on Red Sea Water. *Geophys. Res. Lett.* **29**, 21–24 (2002).
98. Sirocko, F. Ups and downs in the Red Sea. *Nature* **423**, 813–814 (2003).
99. Petschick, R. *MacDiff, Freeware Scientific Graphical Analysis Software for X-ray Diffraction Profiles*. (Frankfurt, 2001).
100. Jarosewich, E., Nelen, J. A. & Norberg, J. A. Reference samples for electron microprobe analysis. *Geostand. Newsl.* **4**, 43–47 (1980).
101. Callahan, B. J. et al. DADA2: high-resolution sample inference from Illumina amplicon data. *Nat. Methods* **13**, 581–583 (2016).
102. Martin, M. Cutadapt removes adapter sequences from high-throughput sequencing reads. *EMBnet J.* **17**, 10–12 (2011).
103. Quast, C. et al. The SILVA ribosomal RNA gene database project: improved data processing and web-based tools. *Nucleic Acids Res.* **41**, D590–D596 (2012).
104. Foster, Z. S., Sharpton, T. J. & Grünwald, N. J. Metacoder: an R package for visualization and manipulation of community taxonomic diversity data. *PLoS Comput. Biol.* **13**, e1005404 (2017).
105. Wickham, H., Chang, W. & Wickham, M. H. Package 'ggplot2' Create Elegant Data Visualisations Using the Grammar of Graphics. Create elegant data visualisations using the Grammar of Graphics. Version 2, 1–189 (2016).
106. RSudio Team. RStudio: Integrated development environment for R (Version 1.4. 1106). *J. Wildl. Manag.* **75**, (2021).

Acknowledgements

The authors would like to thank the captains and crews of RV Azizi, OSS Handin Tide, and RV Aegaeo for their support at sea during the campaigns in 2021, 2022, and 2023. We further appreciate the help of the scientific parties on board the research cruises, particularly the HCMR scientists and the AUV and ROV teams of Fugro and HCMR. We are grateful to KAUST Coastal and marine core labs for organizing the research expeditions and providing technical support on board. NOAA/PMEL provided the MAPRs, and we especially thank Sharon Walker for her support. We are grateful for the technical support at the EPMA provided by Mario Thöner (GEOMAR) and at the SEM of the KAUST Imaging and characterization Corelab provided by Maya Ayach. Cora Schiebener is thanked for helping with the mapping of the fault densities. Figure 3a was designed by Ivan Gromicho (KAUST Research Communication team). We also thank Colin W. Devey (GEOMAR) for his helpful feedback on the paper and the KAUST Research Communication team for proofreading. We thank three anonymous reviewers for their comments and suggestions that improved the quality of the paper and Dr. Clare Davis for editorial handling. This project was funded by KAUST baseline funding and Red Sea Research Center fund FCC/1/1973-43-01. We are further grateful for the ship-time on the OSS Handin Tide and AUV and ROV equipment provided by Fugro and the funding of ship-time on the RV Aegaeo and ROV equipment by KAUST. All research and sampling were permitted by the Kingdom of Saudi Arabia through KAUST Government Affairs.

Author contributions

F.M.Z., N.A., and S.P. designed the study, interpreted the geological results, designed the figures, and wrote the first draft of the paper. F.M.Z., N.A., and J.F. acquired, evaluated, and interpreted all ROV video material and rock samples. F.M.Z. and S.P. prepared and interpreted the rock chemistry. N.A. collected and processed AUV data. S.M.A., J.S., R.S.P., L.S., and A.S.R. collected, analyzed, and interpreted the microbiological samples and contributed to the paper. A.A. and F.B. evaluated the ROV videos for macrofauna and contributed to the paper. F.M.Z., J.F., E.R.G.P., and M.M. performed the MAPR and CTD surveys. S.B.J. performed microprobe volcanic glass analyses. M.O. and B.H.J. evaluated MAPR and CTD data and contributed to the paper. All authors have participated in the writing of the final version of the paper.

Competing interests

The authors declare no competing interests.

Additional information

Supplementary information The online version contains supplementary material available at https://doi.org/10.1038/s43247-023-01169-7.

Correspondence and requests for materials should be addressed to Froukje M. van der Zwan.

Peer review information *Communications Earth & Environment* thanks Kai Tang and the other anonymous reviewer(s) for their contribution to the peer review of this work. Primary Handling Editors: Erin Bertrand and Clare Davis. A peer review file is available.